Supplementary Methods

Overview. An overview figure that summarizes data compilation and analyses steps and their rationale is presented as Fig. S1.

Chl data compilation. Publicly available upper ocean transparency- and in situ-derived total chlorophyll (Chl) measurements were extracted from the National Oceanographic Data Center (NODC), the Worldwide Ocean Optics Database (WOOD), and the Marine Information Research Center (MIRC); (Table S1). All duplicated Chl measurements were removed. These data were collected over the course of a century by different institutions and methods, hence their precision and accuracy may vary. The accuracy of in situ- (Chl_I) and transparency-derived (Chl_T) Chl concentration may be affected by several factors, including weather conditions, instrumentation, collection technique, collection depth, and temporal changes in sampling methodology. Furthermore, all Chl data sources can be subject to errors associated with data transcription and digitization. Both Chl_T and Chl_I data were systematically filtered to remove measurements associated with these sources of error. While some erroneous measurements may possibly persist, analysis indicates that these represent a small fraction of the total measurements and can be considered as random variation.

Only Chl_I collected in the upper 20 m were extracted. Mean Chl values were calculated over depth for each sampling cast to minimize statistical dependence. Following data extraction, we examined Chl_I to investigate the effect of collection methods on their accuracy. Chl collected using underway collection methods contained atypical frequency distributions. The remainder of collection methods yielded log-normal distributions, which are more typical. Since the accuracy of underway data could not be empirically verified they were removed from the analysis (n=110,935).

All nearshore measurements (< 25 m depth or < 1 km from the nearest coastline) were removed from the analysis (n=252,640). Chl values which exceeded >50 mg m^{-3} globally or >5 mg m^{-3} in open ocean waters (> 200 m depth or >200 km from the nearest coastline) were flagged as biologically improbable outliers and removed (n=23,379). Chl measurements were also examined by their accession number (submitting institution) and cast number to determine the proportion of measurements which were outliers within each accession number and cast. If over 25% of measurements within a given accession number were flagged as questionable, all data from that accession number were removed. This same technique was applied to each individual in situ cast. This was aimed at removing data gathered from casts where the instrumentation might not have been calibrated correctly or from accession numbers where systematic data entry errors might have occurred.

Similarity of Chl data. For comparison, Chl_I and Chl_T were individually binned into 0.25° x 0.25° cells. For each cell, monthly mean values were calculated individually for both Chl_I and

Chl_T for each available year. Mean Chl values were calculated using a modified objective weighting algorithm developed for scatterometer data[1,2]. Spatial weighting functions were calculated as,

$$W_{S,ij} = (S^2 - s_{ij}^2)/(S^2 + s_{ij}^2) \tag{1}$$

Where S is the chosen value for the spatial distance scale (0.25°), and s_{ij} is the distance of the *j*th observation from the center of the *i*th cell. Temporal weightings were calculated as,

$$W_{T,kj} = (T_k^2 - t_{kj}^2)/(T_k^2 + t_{kj}^2) \tag{2}$$

Where T is the number of days in the *k*th month, and t_{kj} is the time separation of the *j*th observation from the center of the *k*th month. Weightings were combined for each unique cell and month as,

$$Chl_{i,j,k} = (W_{S,ij} + W_{T,kj})/2 \tag{3}$$

This produces weightings of 1 at the center of the grid point and middle of the month to near 0 at periphery of the cell and ends of the month. Great circle distances between observations and the center of each cell (s_{ij}) were calculated using the Haversine formula[3]. Pearson correlation coefficients were then calculated to examine the strength of the linear relationship between Chl_I and Chl_T. Strong positive relationships were observed between mean Chl_I and Chl_T (r=0.52; P<0.001), with increasing strength through time. The linear relationship was insensitive to proximity to the coast, although the variability in Chl was slightly higher for shelf areas.

To further explore the linear scaling of these data, model II linear regression models were used[4,5]. Model II regression analysis is appropriate when both variables in the regression equation are random (i.e. subject to error). We log-transformed both Chl data sets in order to achieve bivariate normality and fitted major axis (MA) model II regressions to the data. If Chl estimates from the two data sources were identical, one would expect a Pearson correlation coefficient of 1, a linear slope of 1, and an intercept of 0. We observed strong linear relationships between Chl_I and Chl_T in shelf and oceanic regions, and globally (Fig. S2). To further examine spatial patterns of similarity, we extracted the standardized residuals from these regressions fitted to the entire dataset and calculated the absolute mean residual for each 5° x 5° cell. This value corresponds to the average difference between Chl_T and Chl_I, minimizing the confounding effects of spatial and temporal variation. Spatial examination of the mean residuals indicated that there was a greater discrepancy between Chl_I and Chl_T in more coastal areas (Fig. S2b. Excluding more coastal Chl_T measurements had a minor effect on the linear regression statistics and the higher residual variability remained in coastal regions. Linear regression techniques were also used to examine the effects of in situ collection methods on the linear agreement between Chl_T and Chl_I. These differences were negligible.

Blended Chl were compared against satellite-derived Chl concentrations extracted from the Sea-viewing Wide Field-of-view (SeaWiFS; Fig. S3a), and Coastal Zone Color Scanner projects

(CZCS; Fig. S3b). Spatial patterns of the blended Chl data broadly approximated those from remote sensing radiometry and major spatial features such as the oligotrophic gyres, equatorial upwelling, and enhanced phytoplankton production in coastal and high latitude regions were well reproduced (Fig. S3c).

The similarity of Chl_T and Chl_I was also examined using regression trees. Regression trees use recursive partitioning to split data to explain the largest amount of variation possible. Regression trees were fit to each of our 10 focal regions and globally using the main model covariates and a dummy variable (β_D) corresponding to the data type (0=in situ; 1=transparency). This data type variable only appeared in 2 of 11 regression trees and was confined to the lowest branches, indicating that data type explained very little variation in overall Chl concentration.

Estimation of Chl trends. Trends in relative Chl concentration for each ocean region and 10° x 10° cell were estimated from blended data using generalized additive models (GAMs)[6]. GAMs are a flexible extension of generalized linear models that allow the specification of the linear predictor (response) as a generalized linear or smooth function of covariates. This approach can be advantageous when it is suspected that the response varies as a complex non-monotonic function of covariates, or where one expects complex interactions among covariates. The application of GAMs to ecological data is rapidly growing in recently published works, especially in the field of biological oceanography[7-8].

Statistical models

The model covariates were selected to explain the largest proportion of the variation in Chl while remaining parsimonious. Phytoplankton growth and abundance vary spatially and temporally with changes in photosynthetically active radiation and nutrient availability, among other factors. We attempted to explain variability related to these processes by including model covariates for mean seasonality (day or month of the year), the water depth of sampling locations where Chl observations were taken (bathymetry), temporal change (year), and spatial changes (latitude and longitude).

Local-scale Chl trends were estimated by fitting individual GAMs to data in each 10° x 10° cell. For these models, we specified Chl as a linear function of year, as a smooth function of bathymetry, and as a discrete function of month of the year. Spatial Chl variability was explained by using individual smooth functions of latitude and longitude. Following this, local Chl trends for each cell containing adequate data (n=364) were estimated as follows:

$$\eta(\mu_i) = B_0 + B_1 Year_i + B_2 Month_i + f_1(Bathymetry_i) + f_2(Latitude_i) + f_3(Longitude_i) + \epsilon_i \quad (4)$$

where η is the monotonic link function of the expected mean Chl concentration μ_i, B_0 is the model intercept, B_i are parametric and f_i are nonparametric effects estimated from the data and ϵ_i is the model error term. A Gamma distributed error structure and a log link were used.

To estimate regional Chl trends, more abundant data within each basin-scale region (n=10) led to modified covariate specification. For bathymetry, we used a 3-level discrete variable defined as: *i*) less than 200 m, *ii*) between 200 and 1000 m depth, or *iii*) greater than 1000 m). Seasonality relates to variation in both sunlight and nutrients throughout each year. To explain variation in Chl associated with seasonality we assumed that Chl varied as a smooth function of day of the year. This allowed different patterns of seasonality to be fitted within each region. Since many regional patterns of phytoplankton seasonality are well-known (e.g. Arctic, versus temperate and tropical regions), examination of the estimated seasonality patterns provided a useful verification to ensure the model was correctly specifying mean seasonal Chl variability. Statistical dependence, whereby observations are not independently distributed, arises frequently in ecological data. For phytoplankton, spatial dependence not captured by bathymetry or seasonality may be due to physical oceanographic features such as fronts and eddies, or localized enrichment due to upwelling or anthropogenic contributions. A smooth spatial variable (latitude, longitude) was used to capture potential spatial dependence not explained by bathymetry or seasonality. The inclusion of this term also captured variability associated with spatial differences in sampling effort. Regional Chl trends were estimated by fitting GAMs to the blended data in each region, in order to estimate Chl as a log-linear function of time as

$$\eta(\mu_i) = B_0 + B_1 Year_i + B_2 Bathymetry_i + f_1(Day_i) + f_2(Latitude_i, Longitude_i) + \epsilon_i, \tag{5}$$

and to estimate Chl as a log-smooth function of time as

$$\eta(\mu_i) = B_0 + f_1 Year_i + B_2 Bathymetry_i + f_2(Day_i) + f_3(Latitude_i, Longitude_i) + \epsilon_i, \tag{6}$$

Additional details regarding the specification of parametric and nonparametric effects for local and regional models are presented in Table S2.

Global rates of phytoplankton change were derived by estimating the random-effects meta-analytic means across the 10 individual regional estimates[9]. Global rates were estimated as both inverse variance- and geographic area-weighted means, but results obtained by these weightings were almost identical. Inverse variance-weighted means were used for inference.

Additional robustness analyses

Regional trends were estimated for Chl_T and Chl_I separately as a smooth function of time in each region to determine if trends were similar between data types. Despite large differences in the spatial and temporal coverage of the individual data types, estimated regional Chl trends appeared similar (Fig. S4). There were minor discrepancies between trends derived from the two data sources in some regions. These differences were likely the result of limited data availability in these regions, rather than differences between data types. Regional models were also fitted to the blended dataset for global and open ocean areas individually for each region (Fig. S5). Although the overall global rate of change was similar, several Southern Hemisphere region estimates were different in the open oceans. Spatial analysis of the residuals from these regional models indicated more outlying residuals in the Southern Hemisphere (Fig. S5c). An emergent pattern from these analyses is an elevated degree of uncertainty for trends estimated for Southern Hemisphere regions where data availability is relatively low.

Local-scale trends were estimated for Chl_T and Chl_I individually as well (Fig. S6). Despite the variable temporal coverage of the data within each 10° x 10° cell, trends estimated from each data source individually were broadly similar in most areas. The magnitude of change in each cell was generally greater when estimated from Chl_I, which may reflect greater Chl changes over more recent time periods.

After blending in situ and transparency data, the temporal availability of data within each 10° x 10° cell was variable. Following our robustness approach for the regional models, we estimated local-scale trends from blended data using only data since 1950 as well as the full series (Fig. S7). The spatial patterns of Chl trends was largely unchanged. The linear correlation between estimates using all data against those using only data since 1950 was high (r=0.985; P<0.0001), and the estimated direction of temporal change different in only 2% (n=4) of all cells showing statistically significant effects (n=198). Using only data since 1950 resulted in 61% (n=120) of cells showing statistically significant declines and appeared to amplify the trends observed when using all data.

For in situ data, we also tested the effect of Chl sampling depth (m) and temporal changes in sampling methodologies within the local and regional model frameworks. Results indicated that there is little variability in Chl concentration associated with sampling depth within the upper 20 m.

Notes on model inference, specification and diagnostics

Because maximum likelihood (ML) estimation is inappropriate when including smooth functions as model covariates, all GAMs were fit using penalized likelihood (PL) approximation by penalized iteratively re-weighted least squares (P-IRLS). In PL approximation the model negative log likelihood is modified by adding a penalty which is scaled by a smoothing parameter (λ) for each nonlinear function. The λ parameter represents the tradeoff between model fit and model smoothness and is estimated by generalized cross-validation (GCV) or Un-biased Risk Estimation (UBRE). Because overfitting is common when using GCV estimation, the influence of the effective degrees of freedom on nonlinear estimation was inflated by a factor of 1.4 (ref. [10]). All additive and generalized additive models were estimated using the statistical software R (V. 2.10) and packages (mgcv) developed by Wood[11].

Model assumptions were checked for all regions and all individual 10° x 10° cells, and residuals were examined against all covariates to determine if they were adequately specified. Regional model residuals were also examined spatially to examine any factors affecting model fits (Fig. S5c). Most outlying residuals occurred in the Southern Hemisphere, likely reflecting the relative scarcity of data in these regions, rather than improper model specification. The presence of collinearity among model covariates was examined by calculating the variance inflation factor (VIF); (ref. [12]) for all models. VIF values over 5 were considered evidence of collinearity.

Statistical autocorrelation, which violates the assumption of independence among observations, is common in spatio-temporal data sets. If not properly accounted for, autocorrelation can artificially inflate the degrees of freedom and bias the significance test. We accounted for temporal autocorrelation by including a temporal smooth effect and for spatial autocorrelation by including a latitudinal and longitudinal smooth effect within all GAMs. We then tested the effectiveness of these measures by examining the model residuals. If autocorrelation was still present, spatial and temporal patterns would be apparent in the model residuals. Omni-directional semi-variogram and correlogram analyses[13] of model residuals in each region before and after fitting the spatial variable indicated that our modeling approach was very effective at minimizing spatial autocorrelation (Fig. S8a). Although residuals from models without spatial effects exhibited clear spatial structure (Fig. S8b), those from models including spatial effects did not (Fig. S8c). Temporal autocorrelation was examined by calculating the mean model residual at 10-day intervals and fitting temporal autoregressive models. No significant temporal structure was observed in the model residuals.

Physical and climate data and analyses. To calculate the bathymetry associated with each Chl sampling station, we used global gridded bathymetry data (30-arc second resolution), extracted from the General Bathymetric Chart of the Oceans database (GEBCO_08). To calculate the distance from the nearest coastline, we used data extracted from the Global Self-consistent, Hierarchical, High-resolution Shoreline Database (GSHHS v1.10). The bathymetry and distance from the nearest coastline were calculated for each Chl measurement using Generic Mapping Tools software (GMT); (http://gmt.soest.hawaii.edu); (Table S1).

We extracted climate anomalies corresponding to the El Niño Southern Oscillation (ENSO); (Dec-Mar average), the Pacific Decadal Oscillation (PDO), the North Atlantic Oscillation Index (NAO), the Atlantic Multidecadal Oscillation (AMO), the Indian Ocean Dipole Index (IOD), the Arctic Oscillation Index (AOI), and the Antarctic Oscillation Index (AAO) from the standard sources listed in Table S1. The bivariate ENSO index represents reconstructed SST anomalies and Southern Oscillation Index (SOI) anomalies. The IOD represents the normalized anomalous SST gradient between the Western Equatorial Indian (50°E to70°E and 10°S to10°N) and the South Eastern Equatorial Indian Oceans (90°E to 110°E and 10°S to 0°N) termed the Dipole Mode Index (DMO); (ref. [14]). The NAO represents the first principle component from a rotated principle components analysis (RPCA) applied to monthly standardized pressure anomalies across the North Atlantic (20° to 90°N); (ref. [15]). The AMO represents the area-weighted SST average over the North Atlantic (0° to 70°N). The PDO is described by the leading principal component of monthly SST anomalies in the North Pacific Ocean (>20°N). The Arctic Oscillation (AO) index or Northern Annular Mode, represents sea level pressure anomalies across the Arctic and North Atlantic Oceans (>20°N). The Antarctic Oscillation (AAO) index or Southern Annular Mode represents the leading principle component of geopotential height anomalies south of 20°S (ref. [16]). High-pass convolution filters (window=9) were applied to all indices to remove high-frequency variability from the series.

We examined the effects of climate indices by taking yearly model predicted Chl in each of 10 regions (i.e. with seasonal, spatial, and depth effects controlled for), converting these to de-trended, normalized anomalies and cross-correlating them against relevant climate indices in each region.

Sea surface temperature (SST) data were extracted from the Hadley Centre Sea Surface Temperature data set (HadISST; 1899-2009); (ref. [17]). Wind intensity data were extracted from the National Oceans and Atmospheric Administration (NOAA) Objectively Analyzed Air-Sea Fluxes (OAFlux) from the Global Oceans database (1958-2009); (ref. [18]). We calculated mixed layer depth (MLD) from subsurface ocean profiles of temperature and salinity extracted from Hadley EN3 v.2a (Met office; 1950 -2009); (Table S1); (ref. [19]). We used a finite MLD definition based on Δdensity (σ_t) = 0.125 kg m (refs. [3,20,21]). The finite difference criterion was chosen opposed to a gradient criterion to estimate MLD because it has been experimentally shown to be more stable[22]. The initial temperature and density values were chosen at a depth of 10 m to eliminate any potential bias in the profile due to 'skin effects' at the ocean surface[23]. Linear interpolation was used to calculate the exact values for MLD.

Global changes in physical variables were estimated by fitting linear models containing covariates for year and month to data in each 1° x 1° and 10° x 10° cell (Fig. S9). Regional changes were estimated by fitting additive models containing covariates for year, month, and location (latitude, longitude) in each region. Since these data were extracted on a global 180° x 360° grid, each individual 1° x 1° grid cell was area-weighted to account for this. To examine the effects of changing SST, MLD, and wind intensity on Chl, all datasets were merged by location (1° x 1° cell), year, and month, and both local and regional models were re-fitted with a physical driver effect estimated. This approach allows isolation of the effects of physical drivers on Chl while removing variability associated with other model covariates (i.e. year, day, latitude, longitude and depth). Since VIF analysis indicated collinearity among some physical variables, individual models containing each physical variable were fit.

Potential sources of error. Limitations in spatial and temporal data availability increase uncertainty in model inference. In the Southern Hemisphere for instance, confidence intervals were wider, estimates fluctuated more, and model residuals were greater, indicating increased uncertainty in these areas due to a relative scarcity of data. We have accounted for this uncertainty by inverse variance-weighting regional estimates when deriving the global mean Chl trends, and also by providing trend estimates using only post-1950 data for comparison. Despite these measures, the patchy nature of the data remains a potential source of uncertainty, especially in the Southern Hemisphere. Furthermore we note that our regional models estimate Chl trends averaged over larger spatial scales and provided little insight into mesoscale differences in trends. We attempted to partly remedy this issue by estimating 'local-scale' phytoplankton trends at 10° x 10° resolution (Fig. 2). Yet, these local-scale models made spatial comparisons difficult due to the different temporal data coverage among cells. Likewise, inconsistency of temporal sampling effort between provinces and cells raises the possibility that sampling intensity was not adequate to fully resolve temporal changes in some regions.

Another potential source of error may be associated with the change in filters used to separate phytoplankton for the extraction of Chl. The earlier use of Whatman GF/C glass fiber filters may have underestimated the concentration of Chl (ref. [24]). This potential bias is only relevant for in situ data and would result in an apparent increase in Chl. Hence, if there were any biases introduced by changes in filters, it would render our estimates of Chl decline conservative.

Supplementary references

1   Levy, G. & Brown, R. A. A simple objective analysis scheme for scatterometer data. *J. Geophys. Res.* **91**, 5153-5158 (1986).

2   Lewis, M. R., Kuring, N. & Yentsch, C. Global patterns of ocean transparency: implications for the new production of the open ocean. *J. Geophys. Res.* **93**, 6847-6856 (1988).

3   Smart, W. M. *Text-book on spherical astronomy, 6th edition*. (Cambridge University Press, 1960).

4   Legendre, P. & Legendre, L. *Numerical ecology. 2nd English edition* edn, (Elsevier Science, 1998).

5   Sokal, R. R. & Rohlf, F. J. *Biometry - The principles and practice of statistics in biologial research*. (W.H. Freeman, 1995).

6   Hastie, T. & Tibshirani, R. Generalized additive models *Stat. Sci.* **1**, 297-318 (1986).

7   Polovina, J. J., Howell, E. A. & Abecassis, M. Ocean's least productive waters are expanding. *Geophys. Res. Lett.* **35**, L03618 (2008).

8   Walsh, W. A. & Kleiber, P. Generalized additive model and regression tree analyses of blue shark (*Prionace glauca*) catch rates by the Hawaii-based commercial longline fishery. *Fish. Res.* **53**, 115-131 (2001).

9   Cooper, H. & Hedges, L. V. *The handbook of research synthesis*. (Russell Sage Foundation, 1994).

10   Kim, Y. J. & Gu, C. Smoothing spline Gaussian regression: more stable computation via efficient approximation. *J. Roy. Stat. Soc. B Met.* **66**, 337-356 (2004).

11   Wood, S. *Generalized additive models: an introduction with R*. (Chapman & Hall/CRC, 2006).

12   Heiberger, R. & Holland, B. *Statistical analysis and data display: An intermediate course with examples in S-plus, R, and SAS*. (2004).

13   Cressie, N. A. C. *Statistics for spatial data*. (John Wiley & Sons, New York, 1993).

14   Saji, N. H., Goswami, B. N., Vinayachandran, P. N. & Yamagata, T. A dipole mode in the tropical Indian Ocean. *Nature* **401**, 360 - 363 (1999).

15   Barnston, A. G. & Livezey, R. E. Classification, seasonality and persistence of low-frequency atmospheric circulation patterns. *Mon. Wea. Rev.* **115**, 1083-1126 (1987).

16   Thompson, D. W. J. & Wallace, J. M. Annular modes in the extratropical circulation. Part I: Month-to-month variability. *J. Clim.* **13**, 1000-1016 (2000).

17   Rayner, N. A. *et al.* Global analyses of sea surface temperature, sea ice, and night marine air temperature since the late nineteenth century. *J. Geophys. Res.* **108**, 1-37 (2003).

18   Yu, L. Global variations in oceanic evaporation (1958-2005): The role of the changing wind speed. *J. Clim.* **20**, 5375-5390 (2007).

19   Ingleby, B. & Huddleston, M. Quality control of ocean temperature and salinity profiles - historical and real-time data. *J. Marine Syst.* **65**, 158-175 (2007).

20   Levitus, S. *Climatological atlas of the world ocean*. Vol. 13 (U.S. Govt. Print. Off., 1982).

21   Kara, A. B., Rochford, P. A. & Hurlburt, H. E. An optimal definition for ocean mixed layer depth. *J. Geophys. Res.* **105**, 803-821 (2000).

22   Bainerd, K. E. & Gregg, M. C. Surface mixed and mixing layer depths. *Deep-Sea Res. A* **9**, 1521-1543 (1995).

23   Fairall, C. W. *et al.* Cool-skin and warm-layer effects on sea surface temperature. *Geophys. Res. Lett.* **101**, 1295-1308 (1996).

24   Venrick, E. L., Cummings, S. L. & Kemper, C. A. Picoplankton and the resulting bias in chlorophyll retained by traditional glass-fiber filters. *Deep-Sea Res. II* **34**, 1951-1956 (1987).

25   Gordon, H. R., Clark, D. K., Mueller, J. L. & Hovis, W. A. Nimbus-7 coastal zone color scanner: system description and initial imagery. *Science* **210**, 60-66 (1980).

26   McClain, C. R. & Signorini, S. R. Subtropical gyre variability observed by ocean-color satellites. *Deep-Sea Res. II* **51**, 281-301 (2004).

27   Wessel, P. & Smith, H. F. A global self-consistent, heirarchical, high-resolution shoreline database. *J. Geophys. Res.* **101**, 8741-8743 (1996).

28   Smith, C. A. & Sardeshmukh, P. The effect of ENSO on the instraseasonal variance of surface temperature in winter. *Int. J. Clim.* **20**, 1543-1557 (2000).

29   Chen, W. Y. & van den Dool, H. Sensitivity of teleconnection patterns to the sign of their primary action. *Mon. Wea. Rev.* **131**, 2885-2899 (2003).

30   Van den Dool, H., Saha, H. M. S. & Johansson, A. Empirical orthogonal teleconnections. *J. Clim.* **13**, 1421-1435 (2000).

31   Saji, N. H. & Yamagata, T. Structure of SST and surface wind variability during Indian Ocean Dipole mode years: COADS observations. *J. Clim.* **16**, 2735-2751 (2003).

32   Enfield, D. B., Mestas-Nunez, A. M. & Trimble, P. J. The Atlantic Multidecadal Oscillation and its relationship to rainfall and river flows in the continental U.S. *Geophys. Res. Lett.* **28**, 2077-2080 (2001).

33   Zhang, Y., Wallace, J. M. & Battisti, D. S. ENSO-like interdecadal variability: 1900-93. *J. Clim.* **10**, 1004-1020 (1997).

34   Manuta, N. J., Hara, S. R., Zhang, Y., Wallace, J. M. & Francis, R. C. A Pacific interdecadal climate oscillation with impacts on salmon production. *Bull. Am. Meteorol. Soc.* **78**, 1069-1079 (1997).

35   Thompson, D. W. J. & Wallace, J. M. The Arctic Oscillation signature in the wintertime geopotential height and temperature fields. *Geophys. Res. Lett.* **25**, 1297-1300 (1998).

36   Mo, K. Relationships between low-frequency variability in the Southern Hemisphere and sea surface temperature anomalies. *J. Clim.* **13**, 3599-3610 (2000).

Supplementary Table S1 | Data sources.

Parameter	Source	Temporal	Webpage	Ref.
Chl	WOOD	1954-2008	www.wood.jhuapl.edu/wood/	
Chl	NODC	1954-2008	www.nodc.noaa.gov/	
Chl	NASA (CZCS)	1978-1986	http://oceandata.sci.gsfc.nasa.gov	25
Chl	NASA (SeaWiFS)	1997-2009	http://oceandata.sci.gsfc.nasa.gov	26
Transparency	WOOD	1899-2004	www.wood.jhuapl.edu/wood/	
Transparency	NODC	1899-2008	www.nodc.noaa.gov/	
Transparency	MIRC	1899-2008	www.mirc.jha.jp/en/outline.html	
Sea surface temperature	Hadley ISST	1870-2009	http://hadobs.metoffice.com/	17
Wind intensity	OAFlux	1958-2005	http://oaflux.whoi.edu/index.html	18
Temperature/Salinity profiles	Hadley EN3 v.2a	1955-2009	http://hadobs.metoffice.com/	19
Bathymetry	GEBCO	NA	www.gebco.net/	
Coastal distance	NGDC	NA	http://www.ngdc.noaa.gov/mgg/shorelines.html	27
Bivariate ENSO index	NOAA	1871-2001	www.esrl.noaa.gov/psd/data/correlation	28
North Atlantic oscillation	NOAA	1950-2009	www.cpc.noaa.gov/products/precip/Cwlink	15 29 30
Indian Ocean dipole	NOAA	1856-2007	www.jamstec.go.jp/frcgc/research/d1/iod/HTML	14,31
Atlantic multidecadal oscillation	NOAA	1856-2009	www.esrl.noaa.gov/psd/data/timeseries/AMO/	32
Pacific decadal oscillation	JISAO	1900-2009	www.jisao.washington.edu/pdo/PDO.latest	33,34
Arctic oscillation	JISAO	1899-2002	www.jisao.washington.edu/ao	35
Antarctic oscillation	NOAA	1979-2009	www.cpc.ncep.noaa.gov/products/precip/CWlink	36

Supplementary Table S2 | Details of GAM effects estimated in the models.

Model	Effects	Specification
Local	year	continuous*
	bathymetry	discrete*
	day	cyclic spline**
	latitude	cubic spline**
	longitude	cubic spline**
Regional (year as continuous)	year	continuous*
	bathymetry	discrete*
	day	cyclic spline**
	latitude,longitude	tensor product spline**
Regional (year as discrete)	year	discrete*
	bathymetry	discrete*
	day	cyclic spline**
	latitude,longitude	tensor product spline**
Regional (year as smooth)	year	cubic spline**
	bathymetry	discrete*
	day	cyclic spline**
	latitude,longitude	tensor product spline**

Notes: * denotes parametric effects, ** denotes nonparametric effects.

Supplementary Table S3 | Regional trends in Chl estimated by GAMs with a continuous log-linear time trend.

Region	Slope	*SE*	*P*	*R²*	GCV	Min year	Max year
Arctic	-0.010	0.001	<0.0001	0.436	0.814	1899	2003
N Atlantic	-0.008	0.000	<0.0001	0.263	0.933	1903	2006
E Atlantic	-0.013	0.001	<0.0001	0.202	0.963	1911	2003
S Atlantic	-0.018	0.001	<0.0001	0.316	0.952	1911	2003
N Indian	0.002	0.001	0.268	0.281	0.650	1942	1997
S Indian	0.020	0.001	<0.0001	0.714	0.821	1936	2007
N Pacific	-0.004	0.000	<0.0001	0.212	0.782	1907	2008
E Pacific	-0.009	0.000	<0.0001	0.375	0.722	1907	2007
S Pacific	-0.005	0.002	0.037	0.538	0.766	1956	2007
Southern	-0.015	0.002	<0.0001	0.218	0.987	1912	2006

Notes: The slope is the estimated instantaneous linear rate of change in abundance, SE = standard error, P is probability that the slope is not different from zero, R^2= the proportion of variance explained by the covariates, GCV=generalized cross validation score.
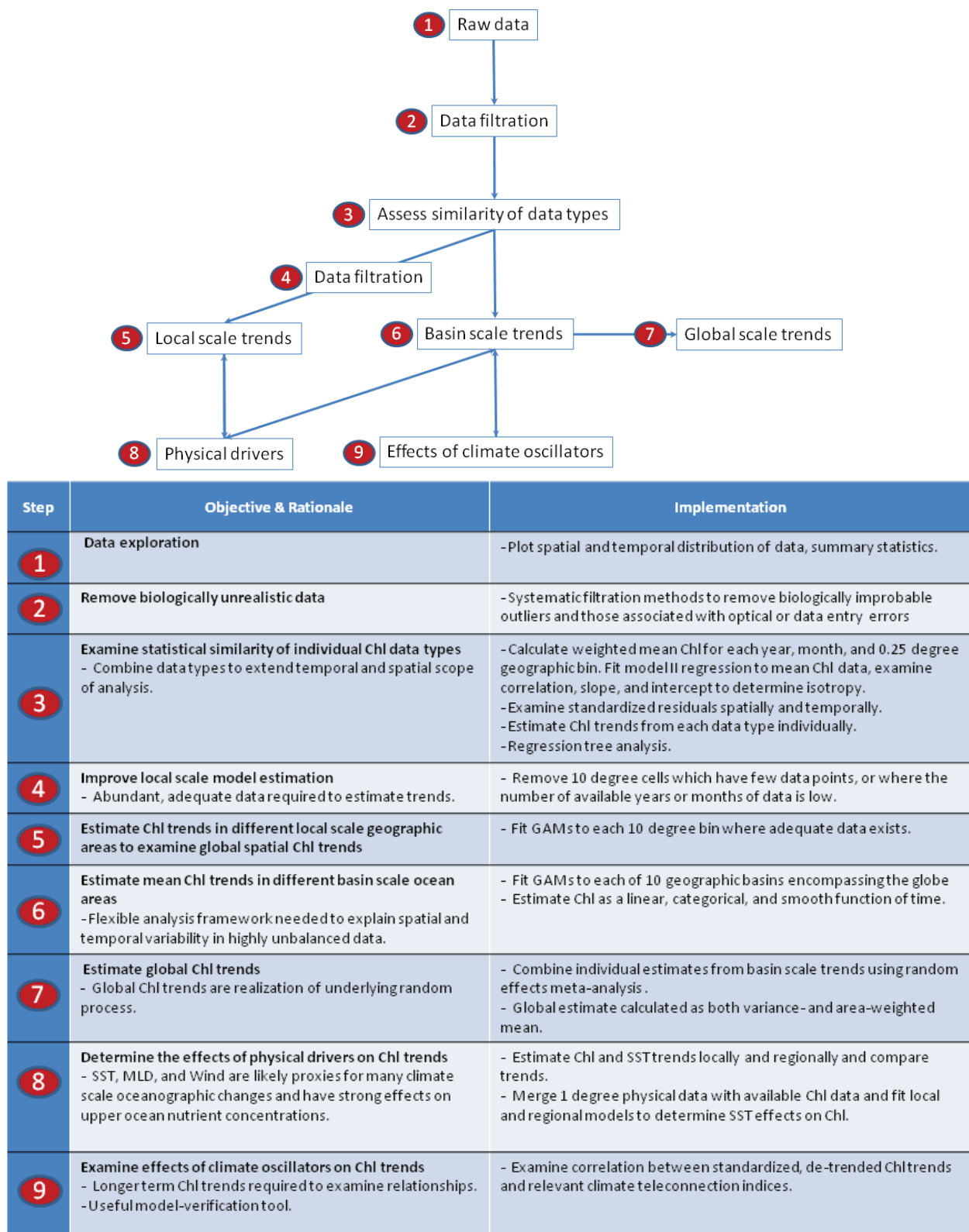
Figure S1 | Schematic of statistical analyses. Flowchart and table depicting the data processing steps, their objectives, rationale, and implementation.
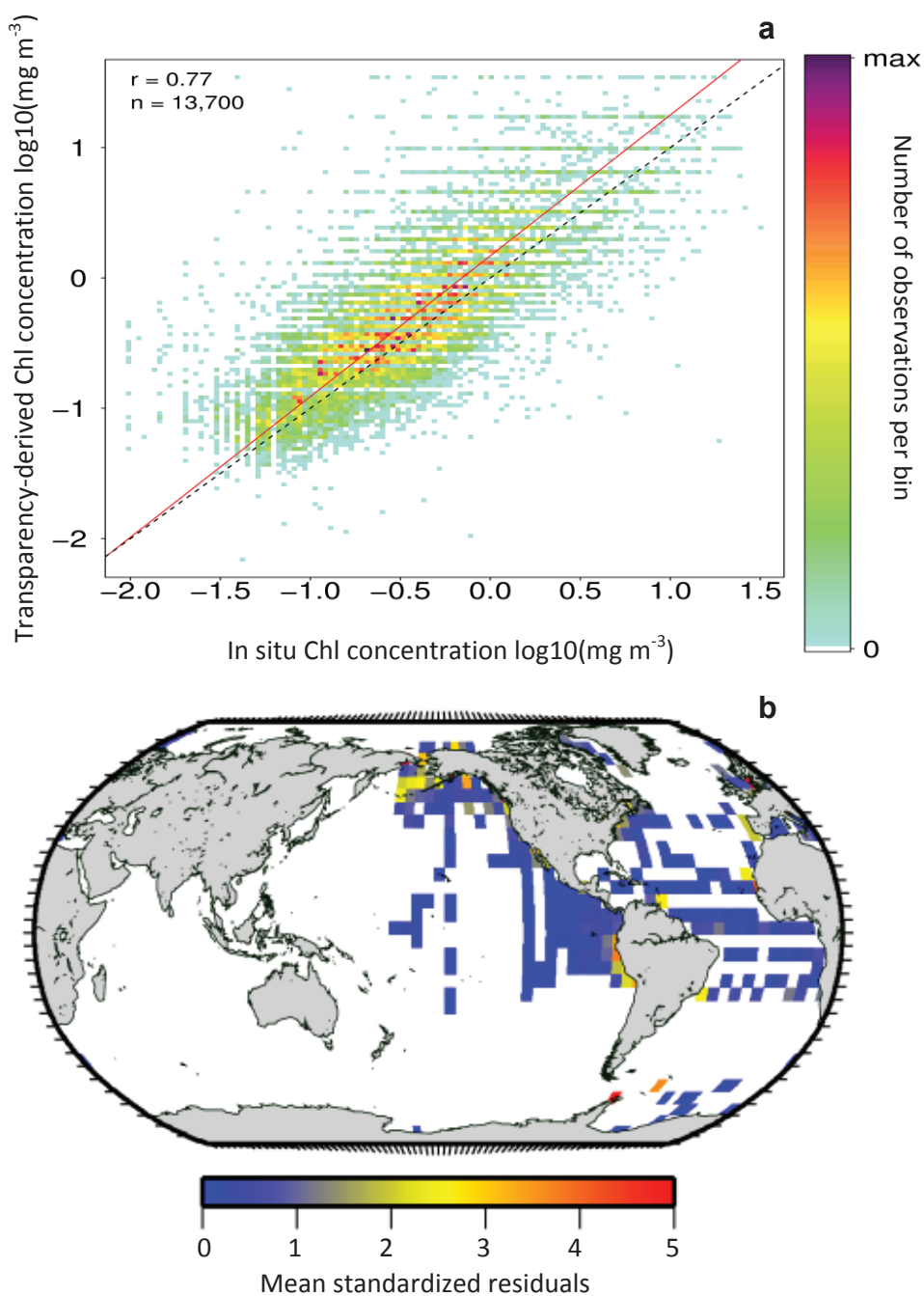
Figure S2 | Comparison between transparency- and in situ-derived Chl data. (a) Linear relationship between transparency- and in situ-derived Chl represented by model II major axis regression model (red line). Points are log10 mean Chl per year, month, and 0.25 degree cell. Color of the points represents the number of observations within each bin. Dashed line represents an idealized slope of 1. Pearson correlation coefficient (r) and sample size (n) are shown. **(b)** Absolute standardized mean model residuals from linear models in **(a)** binned to 5 degree cells. White areas are cells where no matchups exist.
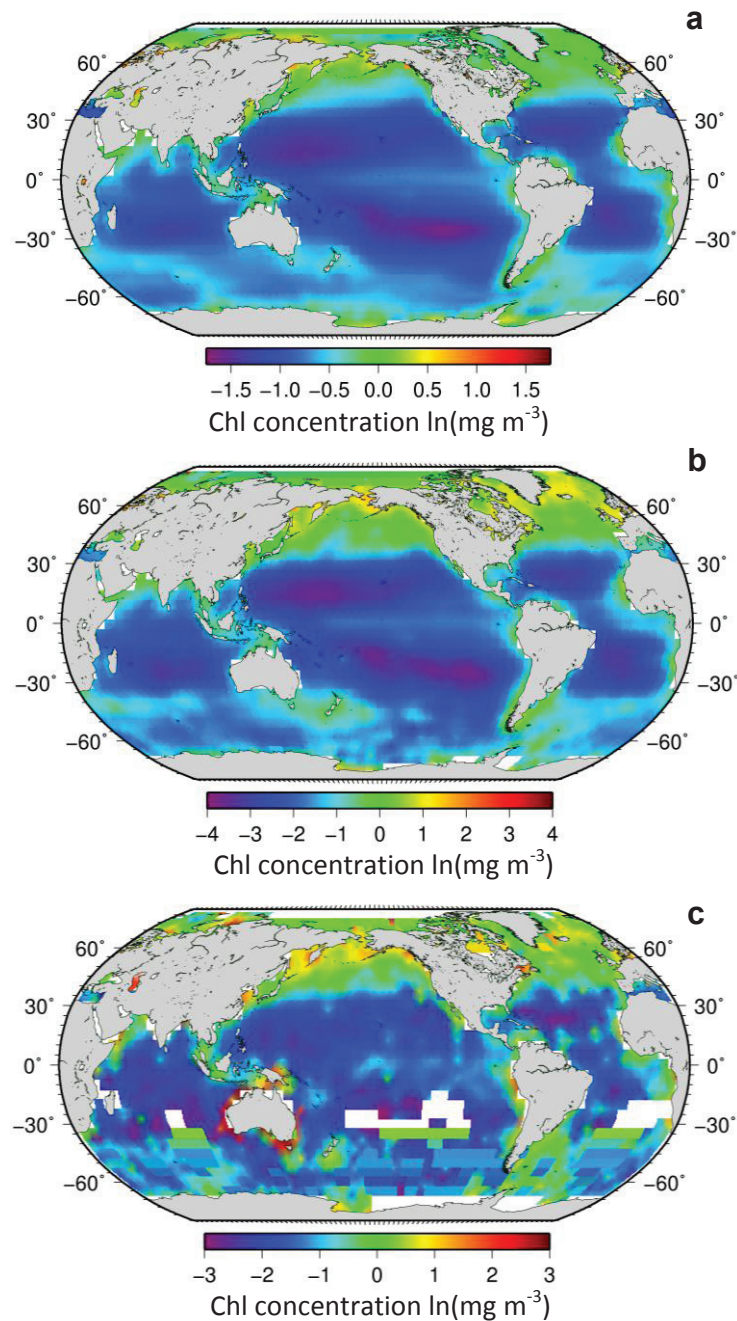
Figure S3 | Chl climatology comparisons. (a-c) Averaged Chl concentration derived from **(a)** the Sea-viewing Wide Field of view Sensor (SeaWiFS), **(b)** the Coastal Zone Color Scanner (CZCS), and **(c)** blended transparency and in situ data. All data were log-transformed and averaged per 5 degree cell for comparison. Seasonal effects were not removed.
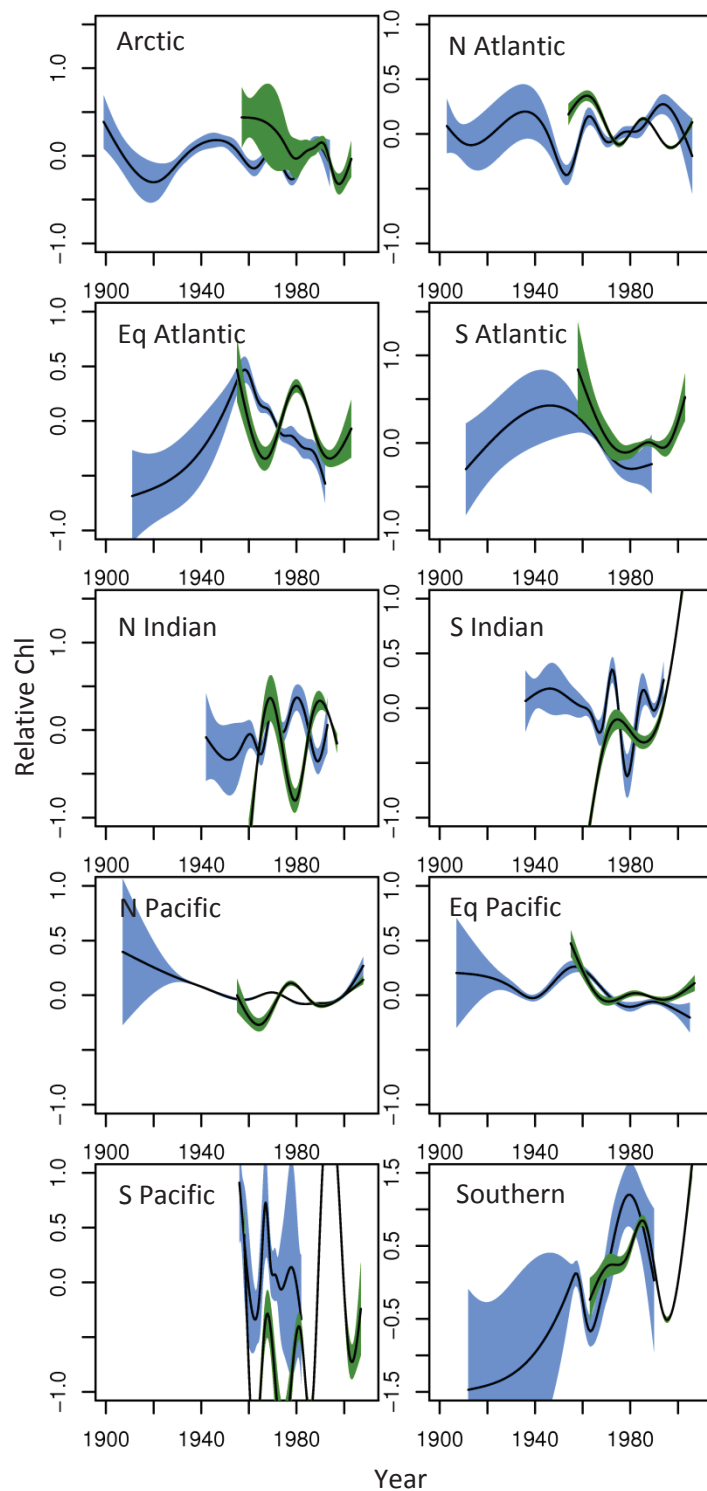
Figure S4 | Regional Chl trends by data source. Estimated smooth rates of Chl change from GAM models fitted to each data source (n=2) and basin (n=10). Blue colors indicate trends estimated using transparency data and green using in situ data. Shaded areas are the 95% confidence limits for each trend.
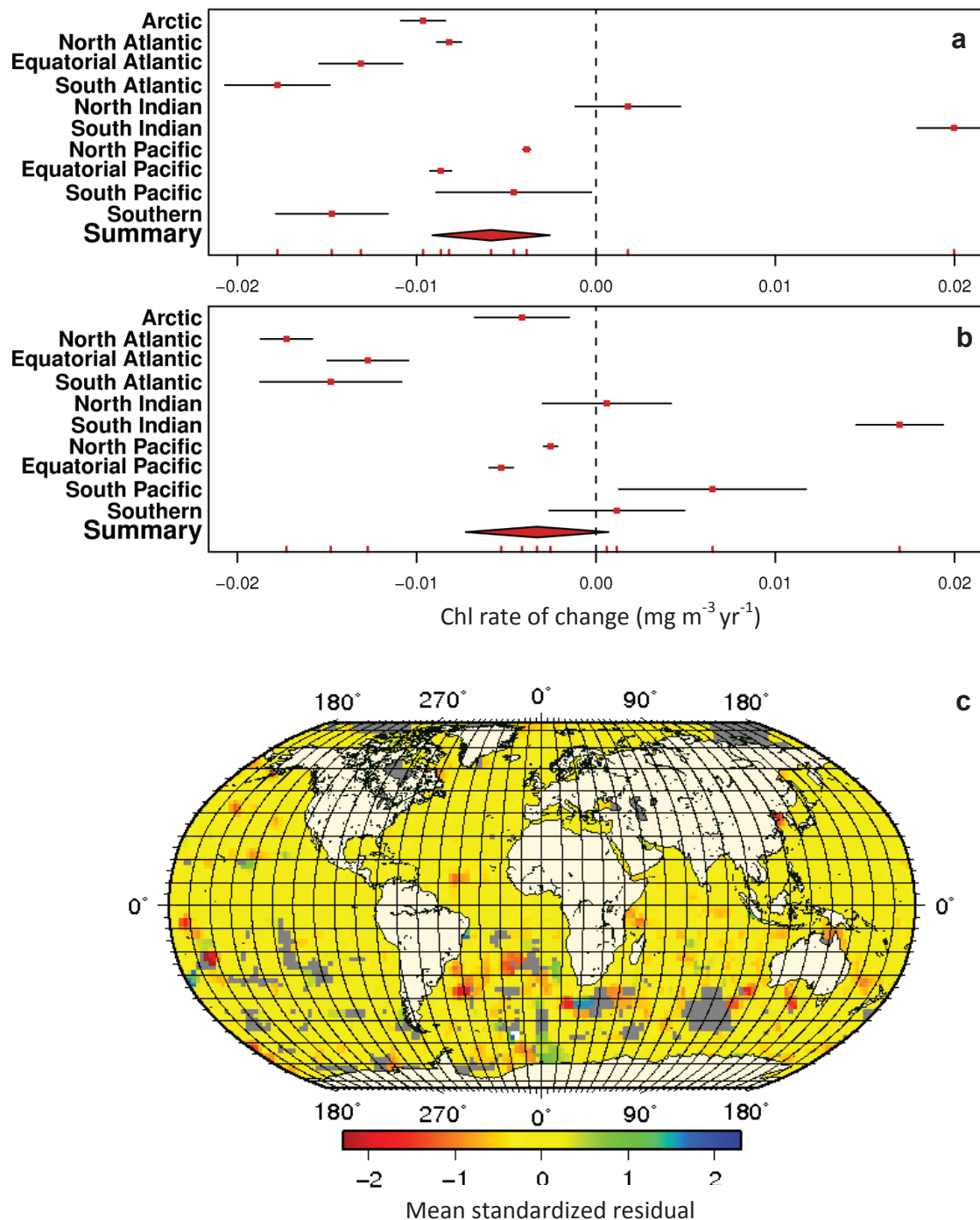
Figure S5 | Regional Chl trends by ocean zone. Estimated rates of Chl change in each region (n=10) from GAM models fitted to all available data **(a)**, and using data in open ocean areas, where water depths are >200 m **(b)**. Means and 95% confidence intervals are shown. **(c)** Mean standardized residuals from 10 regional models in **(a)** plotted on a 1˚ X 1˚ degree grid. Colors depict the mean magnitude of unexplained residual variation in each cell. Grey colors depict missing data.
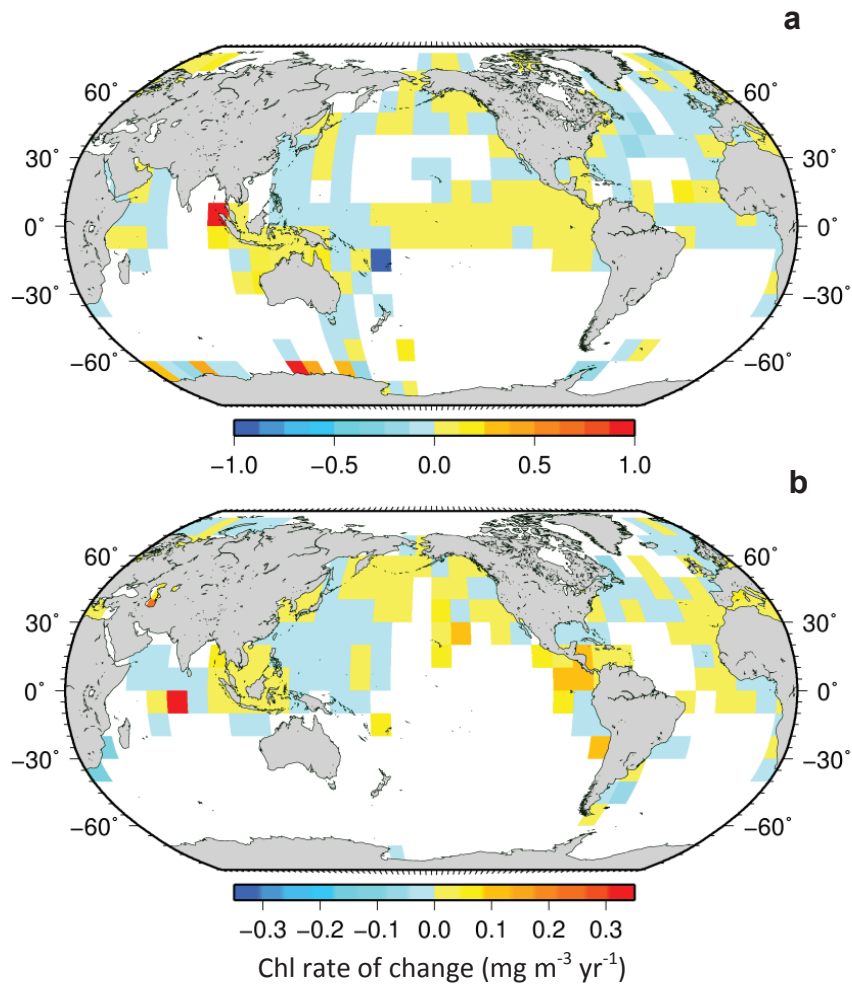
Figure S6 | Local Chl trends separated by data source. Mean instantaneous rates of Chl change estimated for each 10˚x10˚ cell containing adequate data. Trends were estimated for in situ **(a)** and transparency data **(b)**. Yellow and red represent cells where Chl concentration has increased, blue represents Chl decrease, and white indicates cells lacking sufficient data.
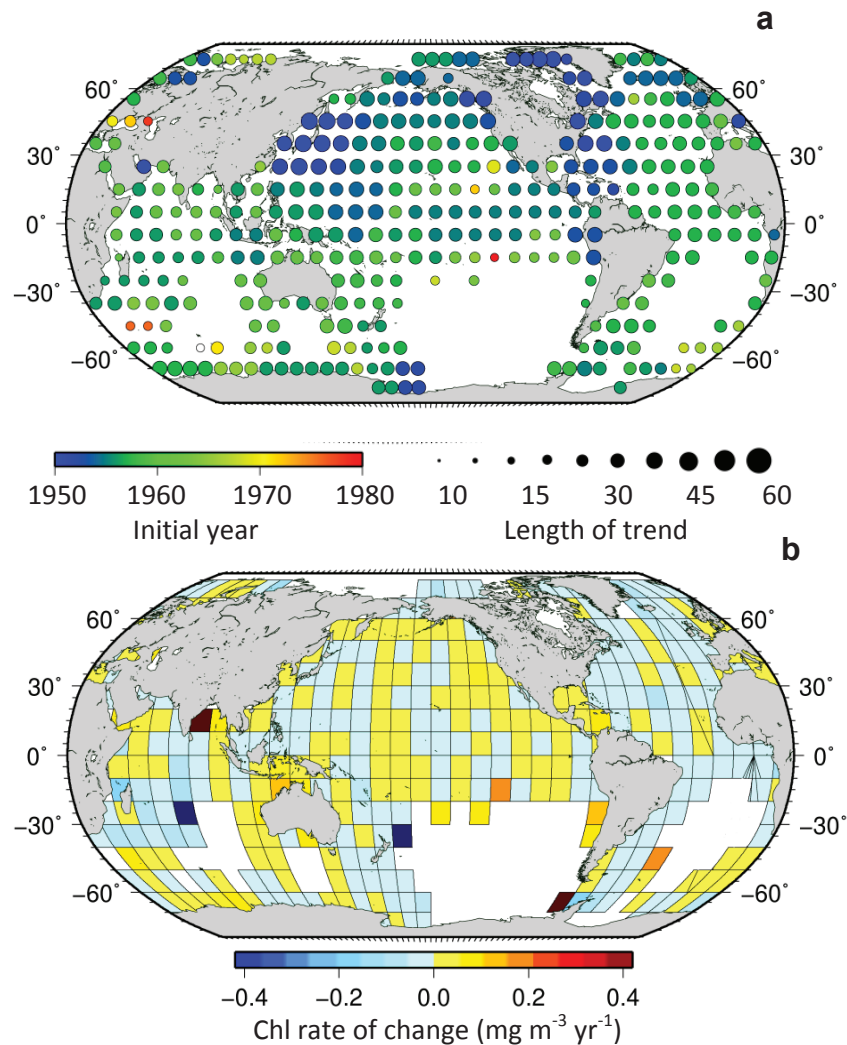
Figure S7 | Spatial variability in phytoplankton trends using post-1950 data. (a) Baseline year and temporal span of Chl data used in local models. **(b)** Mean instantaneous rates of Chl change estimated for each 10˚ x 10˚ cell (squares; n=358). Yellow and red indicate cells where Chl concentration has increased, blue indicates Chl decrease, and white indicates cells lacking sufficient data. Cells bordered in black denote statistically significant rates of change (P<0.05).
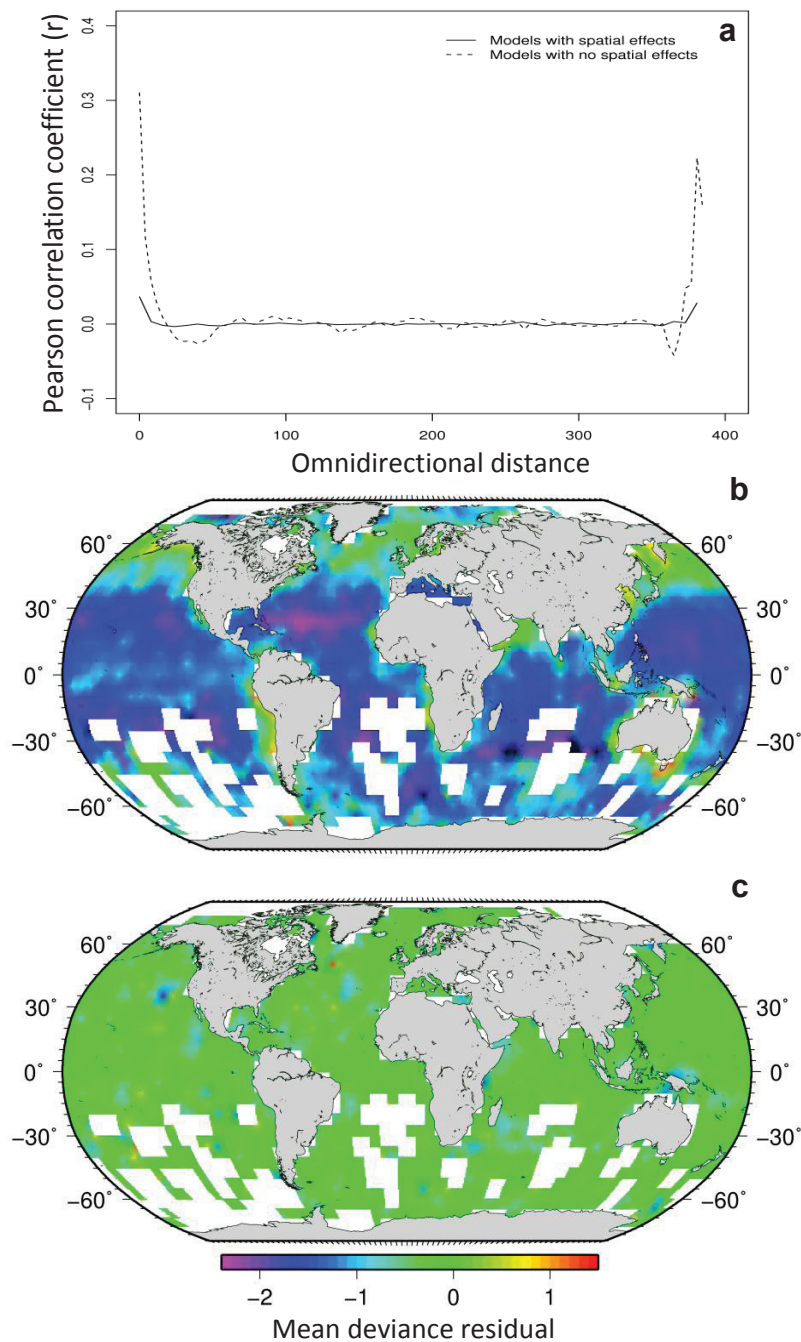
Figure S8 | Effects of removing spatial autocorrelation. (a) Omnidirectional correlogram analysis of mean model residuals from all regional models per 1° cell before (dashed line) and after (solid line) including the spatial effect. **(b-c)** Spatial examination of regional GAM residuals before **(b)** and after **(c)** including the spatial effect. Colors depict the mean model residual in each 1° X 1° cell.
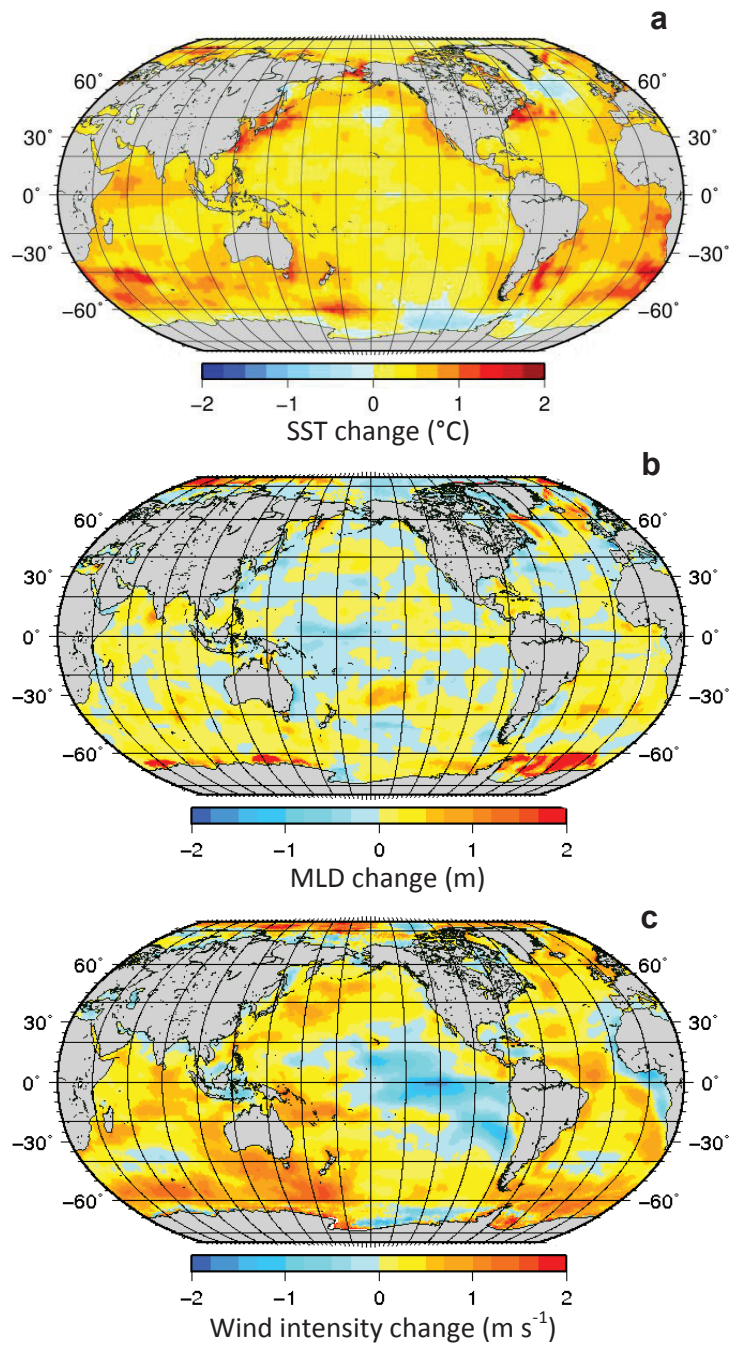
Figure S9 | Physical drivers. (a) Estimated changes in SST (1° resolution 1899-2009), **(b)** MLD (1° resolution 1955-2009), and **(c)** Wind intensity (1° resolution 1958-2009) over the available time periods. Blue depicts declines and yellow and red depict increases.